SAND2014-16681C

Time Resolved Photo-luminescent Decay Measurements of Infrared Materials

September 2014

Grant Soehnel

Sandia National Laboratories
1515 Eubank SE
Albuquerque, NM 87123

ABSTRACT

An experiment has been developed at Sandia National Laboratories that can time resolve the photo-luminescent decay from direct band gap infrared materials. A pulsed laser is used as an excitation source, and the photons resulting from radiative recombination in the sample under test are focused onto a fast photodiode. The optics have a working distance such that the sample under test can be housed inside a Dewar. The laser excitation uses small spot sizes (50-500μm), and the system is mounted on motorized stages so the measurement can be spatially scanned over the area of the sample under test. This has produced detailed carrier lifetime maps over the surface of 4 engineering grade mercury cadmium telluride (MCT) focal plane arrays (FPAs). These maps show strong correlation with FPA properties such as dark current and relative response. The significance is that the measurement is passive (the FPAs are not powered or operating), so it can be used to measure the quality of detectors before hybridization with readout circuitry or material samples.

Keywords: Minority carrier lifetime, time resolved photo-luminescent decay (TRPL), mercury cadmium telluride (MCT), dark current, defects

1.0 Introduction

Photo-sensitive materials have energy states that electrons can move between defined as the valence band (E_v) and conduction band (E_c) [1, 2]. Electrons in the conduction band produce the photo-current that devices use to sense light. Electrons can jump to the conduction band either spontaneously from the thermal energy of the material, or from the absorption of a photon. They leave behind a hole in the valence band. Both electrons and holes are known as charge carriers. Electrons can fall back to the valence band spontaneously through 3 different mechanisms shown in Figure 1. Radiative recombination occurs when an electron falls to the valence band emitting a photon in the process. Some of these photons can exit the material sample and be detected which is the basis for the photo-luminescent decay measurement reported in this paper. SRH recombination occurs when an impurity creates an intermediate energy state known as a trapping level (E_t) which provides a path for the electron to fall to the valence band without emitting a photon. Finally, auger recombination occurs when 2 or more carriers in the conduction band collide causing one to jump to an even higher energy state while the other drops to the valence band without emitting a photon.

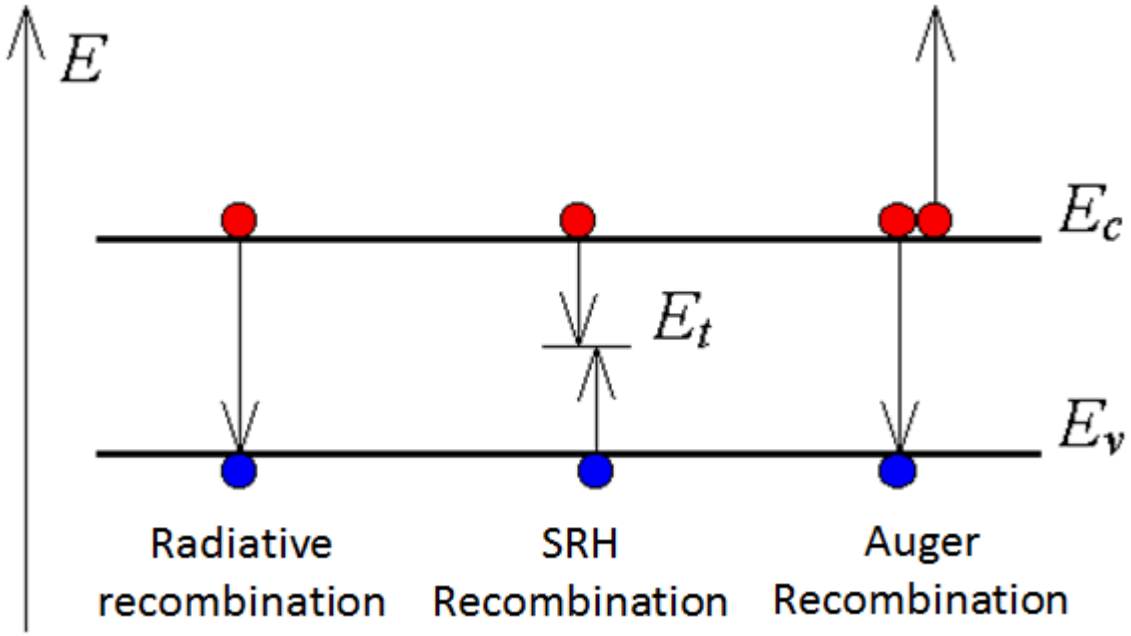

Figure 1: Illustration of the 3 types of carrier recombination

Each of the 3 carrier recombination mechanisms is characterized by a coefficient describing the rate of recombination as a function of the carrier density. The carrier lifetime is determined by the recombination rate(s), and all 3 mechanisms combine to produce an overall lifetime given by [3]

$$\frac{1}{\tau_{total}} = \frac{1}{\tau_{rad}} + \frac{1}{\tau_{SRH}} + \frac{1}{\tau_{aug}}$$

The radiative and auger lifetimes are intrinsic meaning they are fixed and can be calculated theoretically for a given material. The SRH lifetime is dependent on the impurity concentrations in a material and varies from batch to batch and even spatially within a device.

1.1. Carrier recombination model

The modeling and experimental work reported here was performed on fully functional mercury cadmium telluride (MCT) focal plane arrays (FPAs). The material is grown as an alloy in which the Cadmium concentration is set by the parameter "x" which configures the bandgap in $Hg_{(1-x)}Cd_xTe$. Radiative recombination produces photons near the bandgap which as a function of the Cadmium concentration x and the temperature T is defined as [4]

$$E_g = -0.302 + 1.93 \cdot x + 5.35 \cdot 10^{-4} \cdot T(1 - 2x) - 0.81 \cdot x^2 + 0.832 \cdot x^3$$

The intrinsic carrier concentration n_i is the number of electrons (and also holes) for an undoped semiconductor which is given by [5]

$$n_i = (5.585 - 3.82 \cdot x + 1.753 \cdot 10^{-3} \cdot T - 1.364 \cdot 10^{-3} \cdot x \cdot T) \cdot 10^{14} \cdot E_g^{\frac{3}{4}} \cdot T^{\frac{3}{2}} \cdot \exp(\frac{-E_g}{2 \cdot k \cdot T})$$

where k is Boltzmann's constant. Doping intentionally adds impurities that provide excess electrons (n-type doping) or holes (p-type doping). This causes the material to deviate from having equal numbers of electrons and holes in equilibrium. For doped materials, the general equations for the equilibrium concentrations of electrons and holes n_0 and p_0 are

$$n_0 = \frac{N_D - N_A}{2} + \sqrt{\left(\frac{N_D - N_A}{2}\right)^2 + n_i^2}$$

$$p_0 = \frac{N_A - N_D}{2} + \sqrt{\left(\frac{N_A - N_D}{2}\right)^2 + n_i^2}$$

where N_D and N_A are the doping concentrations of donor and acceptor ions respectively. The following equation also holds true regardless of the doping concentrations [1]

$$n_0 p_0 = n_i^2$$

These equations determine the initial steady state concentration of electrons and holes in the absence of any optical excitation. The following equation can be used to determine the total rate of change of carriers in a sample that is not at equilibrium

$$\frac{\partial n}{\partial t} = \frac{\partial p}{\partial t} = G_{optical} - (U_{aug} + U_{rad} + U_{SRH})$$

where n and p are the electron and hole concentrations, $G_{optical}$ is the rate of carriers generated due to an optical excitation, and U_{aug}, U_{rad}, and U_{SRH} are the net recombination rates due to the auger, radiative, and SRH mechanisms respectively. The net recombination rate takes into account the spontaneous generation rate of electron-hole pairs. Equations for the net recombination rates are as follows [3]:

$$U_{aug} = C_n(n^2 p - n_0^2 p_0) + C_p(np^2 - n_0 p_0^2)$$

$$U_{rad} = B(np - n_i^2)$$

$$U_{SRH} = \frac{(np - n_i^2)}{\tau_{SRH-n}(p + p_1) + \tau_{SRH-p}(n + n_1)}$$

where C_n and C_p are auger recombination rate coefficients, B is the radiative recombination rate coefficient, τ_{SRH-n} and τ_{SRH-p} are SRH capture time constants for electrons and holes, and p_1 and n_1 are SRH densities. The SRH densities depend on the trap level E_t, and without any knowledge of the nature of the impurities and defect states, we invoke the assumption that the trap level is equal to the

Fermi level which sets $n_1 = n_0$ and $p_1 = p_0$. The radiative and auger recombination rates for MCT can be calculated for a given temperature and cadmium concentration [6,7]. The SRH capture time constants are set equal to each other for this study due to lack of knowledge of the nature of the possible defects. This creates one parameter related to the SRH lifetime that is of key interest because it is what varies depending on the material quality.

The carrier recombination simulation is performed numerically by the following equations

$$n(t + \Delta t) = n(t) + \Delta t \cdot G_{optical} - \Delta t \cdot (U_{aug} + U_{rad} + U_{SRH})$$

$$p(t + \Delta t) = p(t) + \Delta t \cdot G_{optical} - \Delta t \cdot (U_{aug} + U_{rad} + U_{SRH})$$

where the time step Δt varies based on the current total rate so that the carrier concentration does not change too much for any single step. Figure 2 shows an example of the simulation for a 10ns laser pulse exciting a 0.5mm circular area with 1nJ of total energy. The material simulated is MCT at a temperature of 100K and the cadmium concentration is 0.287. Note that the auger recombination rate equation has the highest order terms with respect to the carrier concentration, so it becomes dominant for high concentrations immediately after the laser pulse. The recombination coefficients and carrier concentration generally causes a shift from auger recombination being dominant, to radiative, and finally to SRH recombination.

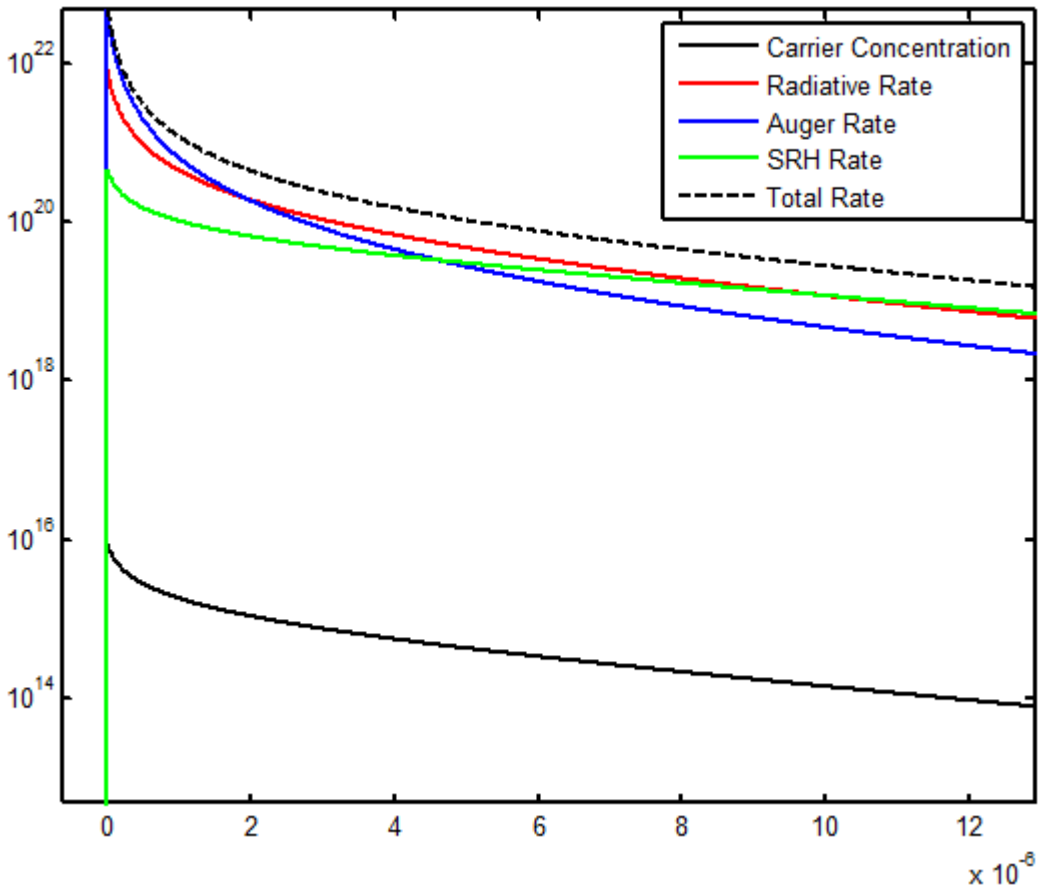

Figure 2: Simulation of carrier recombination with a 10ns laser pulse. Spot size is 0.5mm, and energy of the pulse is 1nJ. The material is MCT at 100K and cadmium concentration of 0.287

1.2. Time resolved photo-luminescent decay measurement

A diagram of the photo-luminescent decay experiment is shown in Figure 3. The laser is an Ekspla OPO tunable from 2500-4450nm with a 500Hz repetition rate. The wavelength used for these experiments is 2500nm. The laser is coupled into a fiber which is mounted along with all the other optics on motorized stages in an XYZ configuration (dashed box). A beam splitter with ~10% reflectance is used to direct the fiber output towards the Dewar and FPA under test. The system is configured this way so that the photo-luminescent light exiting the FPA passes through the beam splitter with ~90% transmission. Filters are used to block any stray or reflected laser light, and the photo-luminescent return (which has been wavelength shifted to the band gap of the FPA) is focused onto a 1mm diameter MCT photodiode from Kolmar Technologies. The photodiode output is read with an oscilloscope which is set to average mode to collect and average the decay from 512 laser pulses to boost the SNR. The motorized stages are used to scan the excitation laterally across the sample, and can also be used to focus/defocus the excitation spot from the laser to change the spot diameter. 2D scans over the FPAs under test were generally performed with 0.5mm spot sizes with the scan step size equal to the spot size. The FPAs are 38X38mm requiring ~4600 scan steps. The full 2D scan can be completed in ~2.5 hours. The time required per scan step consists of a fixed overhead to move the stages, and then whatever time is required to collect the desired number of oscilloscope traces to average at each step. The SNR can be improved further by averaging more than 512 traces, but the scan time goes up proportionally. High resolution scans were performed over smaller areas of interest at spot sizes of 0.15mm and 0.05mm.

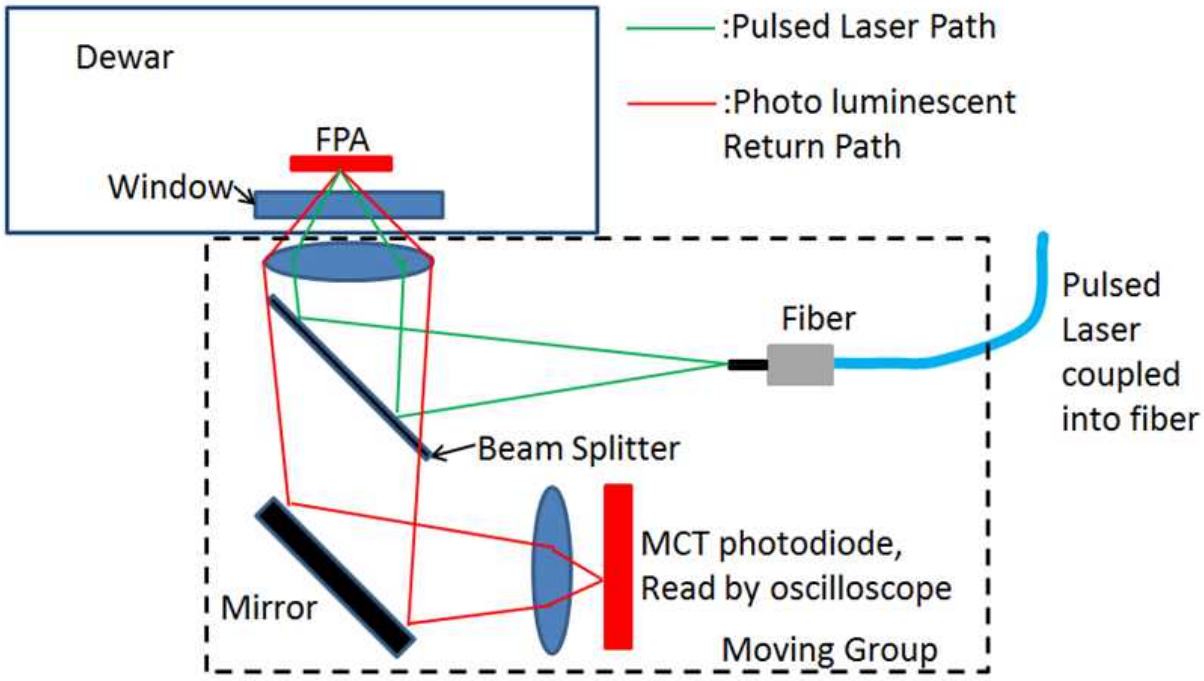

Figure 3: Diagram of the photo-luminescent decay experiment

The oscilloscope traces measured with the experiment are directly proportional to the radiative recombination rate. The challenge to interpreting the data is that the SRH lifetime is the parameter of interest and all 3 recombination mechanisms affect the overall decay after the laser pulse. In addition, the lab data has a noise floor associated with it. In order to use all the information contained in the oscilloscope traces, the simulation was configured as an optimization problem where the metric is a measure of the error between the oscilloscope trace and the radiative recombination rate as a function of

time from the simulation. The radiative rate from the simulation is scaled to the oscilloscope trace. Figure 4 shows 3 oscilloscope traces and the simulation optimized fit. The fit is performed starting 500ns after the laser pulse to avoid any inaccuracies around the laser pulse itself caused by the response time of the detector and any stray laser light still reaching the detector despite the spectral filtering. Time 0 on the plot is actually 500ns after the laser pulse. This starting time has been varied from 100-500ns after the pulse depending on the lifetimes of the sample under test. The data before the laser pulse is used to determine the noise floor, and that is included in the simulation. The simulation is optimized using the Matlab function fminsearch, and the SRH lifetime and initial carrier concentration are set as variables. The flexibility exists to make other material parameters (auger and radiative rates, intrinsic carrier concentration) variable as well, but they were fixed according to their theoretical values in this study.

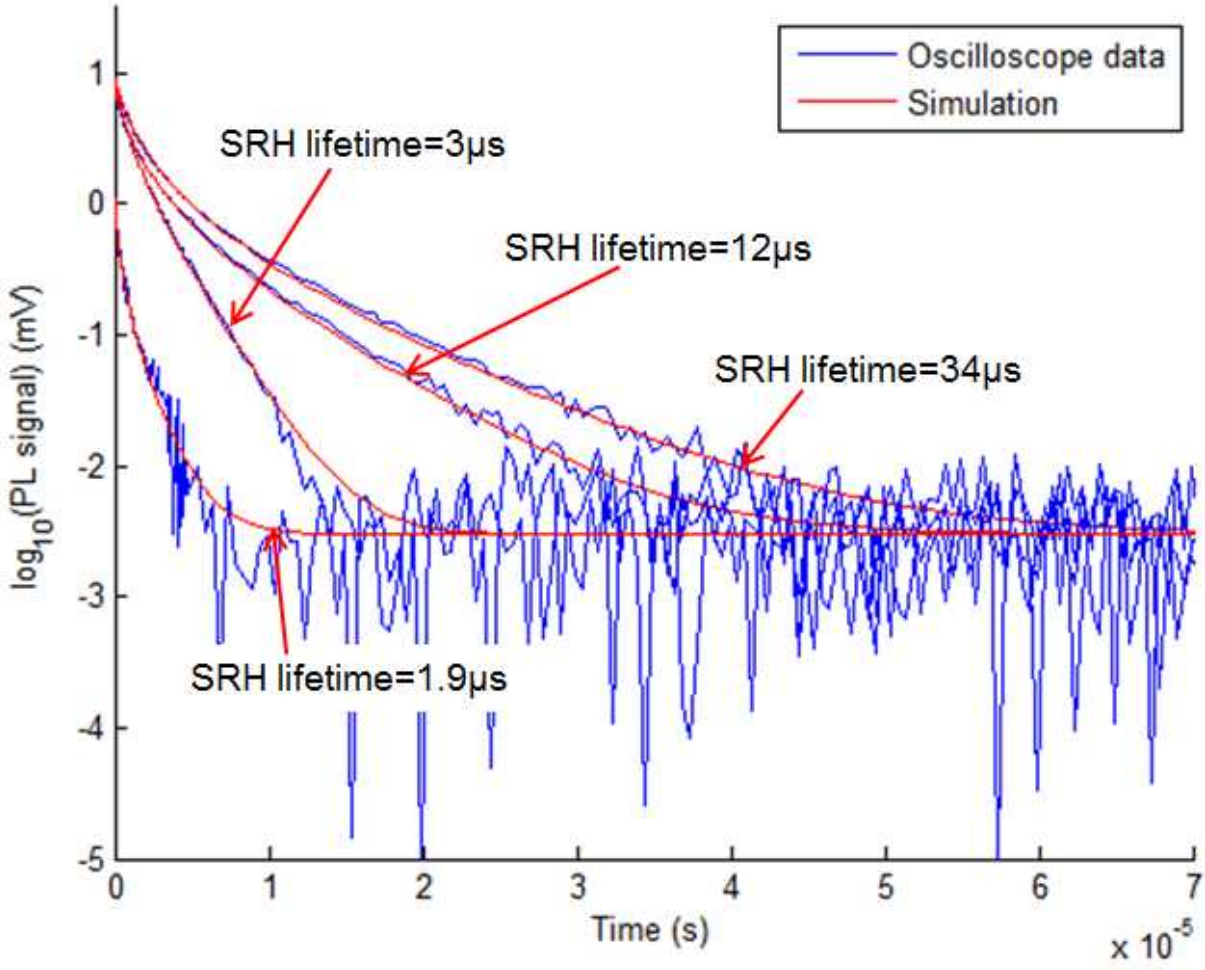

Figure 4: Example oscilloscope traces and simulation optimized fit for 3 different FPA locations and SRH lifetimes

A challenge of measuring the photo-luminescent decay is that the SNR is generally low. Increasing the laser excitation power generally does very little to improve the measurement. Figure 5 shows simulated oscilloscope decay traces with the laser power at 0.5nJ and 5nJ for a range of SRH lifetimes. The very short duration initial peak of the signal is much higher at the higher laser power. However, the later time range in which SRH lifetimes become distinct from one another is barely affected. This is because the higher laser power is creating a very high initial carrier density which causes the auger recombination rate to be very fast. This added power decays very quickly from auger recombination leaving the rest of the decay slope and shape relatively unchanged.

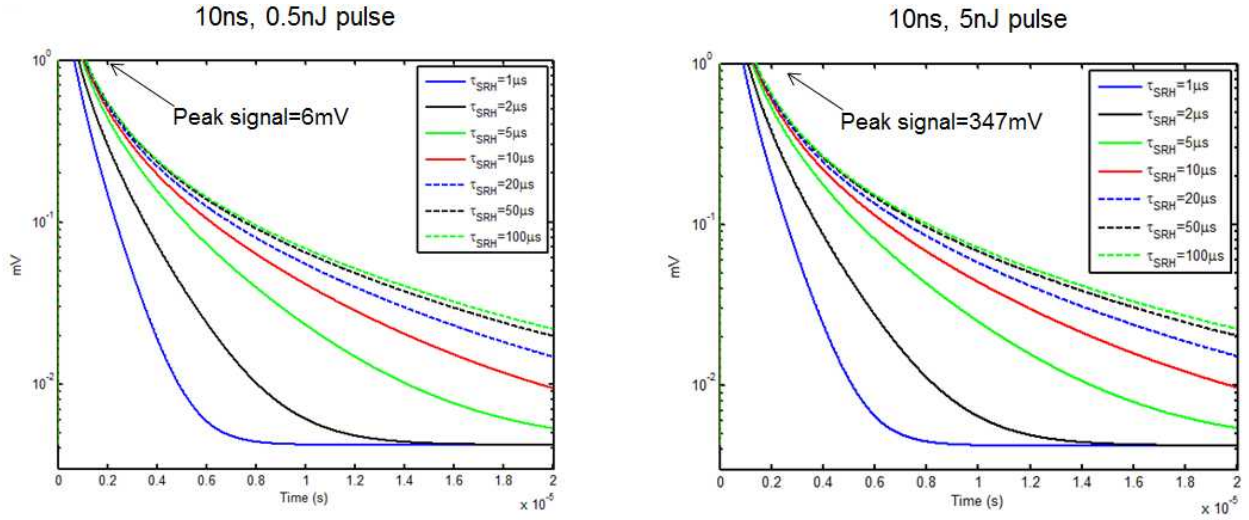

Figure 5: Comparison of simulated oscilloscope decay traces with a 0.5nJ and 5nJ pulse for a range of SRH lifetimes. Spot diameter is 0.5mm.

The low utility of increasing laser power also explains why using smaller excitation spot sizes reduces the SNR. Figure 6 shows a comparison of simulated oscilloscope traces with a spot diameter of 0.5mm and 0.15mm at the same laser power. The laser is more concentrated at a spot diameter of 0.15mm, so the initial carrier concentration is higher. This higher initial peak decays quickly before significant differences due to the SRH lifetimes become apparent. Note that the signals once the SRH lifetimes begin to spread apart are all scaled lower with the smaller spot size. This is because there is less volume of material excited. The recombination rates may be the same as with the 0.5mm spot diameter, but exciting less volume produces less total signal (radiative photons) leaving the sample.

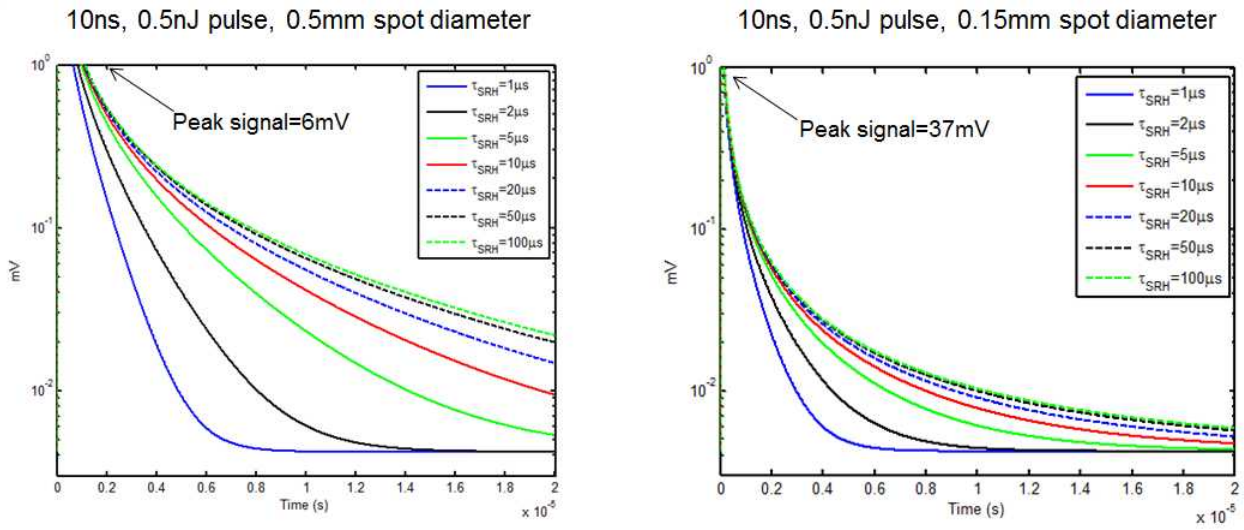

Figure 6: Comparison of simulated oscilloscope decay traces with a 0.5mm and 0.15mm excitation spot diameter for a range of SRH lifetimes

2.0 Results

The lab measurement was performed on 4 2Kx2K engineering grade MCT FPAs that have many known defects, areas of high dark current, and poor response with the intent of observing correlation between these things and the SRH lifetime. 2 of the FPAs have a shortwave cutoff (SWIR) at ~3.6µm, and 2 have a midwave cutoff (MWIR) at ~5.5µm.

Figure 7 shows the lifetime map (SRH lifetime) and corresponding dark current map over the entire surface of SWIR FPA #1. The spot size and scan step size for the lifetime map was 0.5mm. All of the general spatial features of the lifetime map have a strong correlation in the dark current map. Note lifetime is inversely proportional to dark current. A short lifetime indicates high levels of impurity which in turn produces a high dark current. Figure 8 contains high resolution lifetime maps of an area of interest (black box of Figure 7) that had particularly dense spatial features. Those features are increasingly resolved, even at the 0.05mm spot size. Smaller spot sizes produce less photo-luminescent return because the volume of material excited is less, so the SNR gets worse. Smaller spot sizes are most effective when scanning over an area with short lifetimes which are easier to resolve in the simulation.

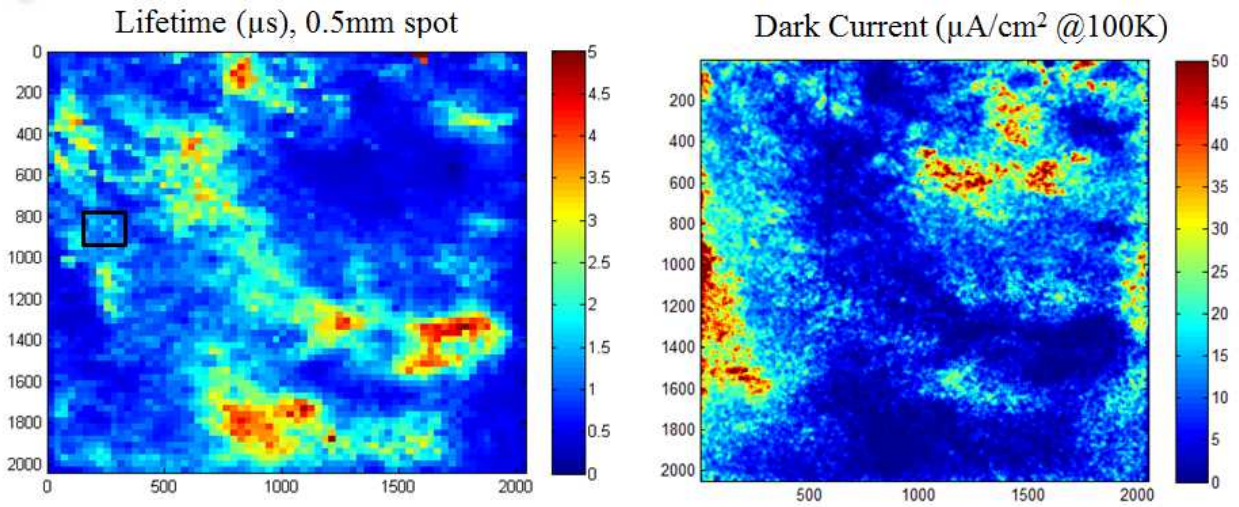

Figure 7: Lifetime (µs) and dark current maps for SWIR FPA #1

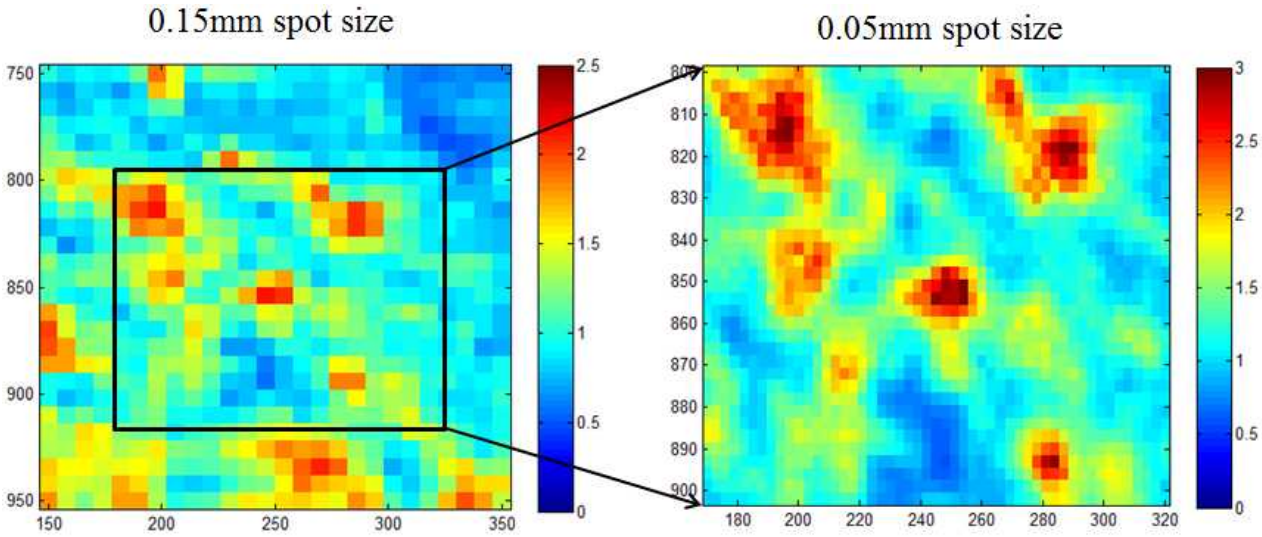

Figure 8: Higher resolution lifetime maps (µs) for SWIR FPA #1 area of interest

There was one region in SWIR FPA #1 in which the lifetime was the lowest anywhere on the 4 FPAs tested. This region along with the corresponding relative response is shown in Figure 9. The lifetime is so short in the center of the defect (~100ns), that a charge diffusion simulation previously developed indicated that the QE would be affected due to the extremely high rate of carrier recombination as shown in Figure 10. The relative response map confirms that the QE is affected within this defect with the minimum QE at ~0.5.

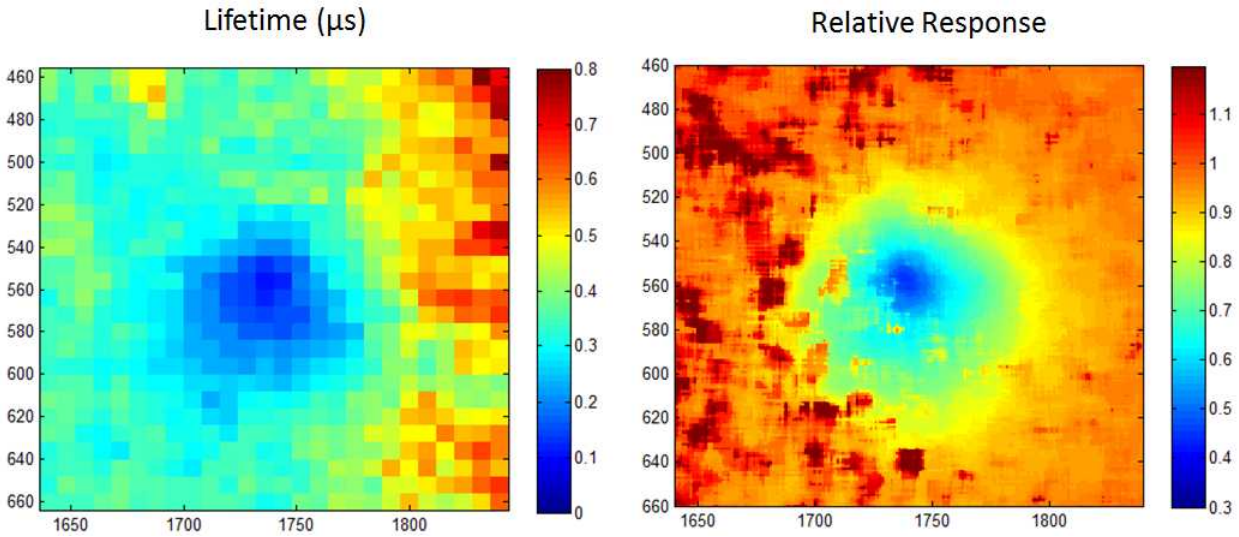

Figure 9: Defect on SWIR FPA #1 in which the relative response is affected by the short lifetime

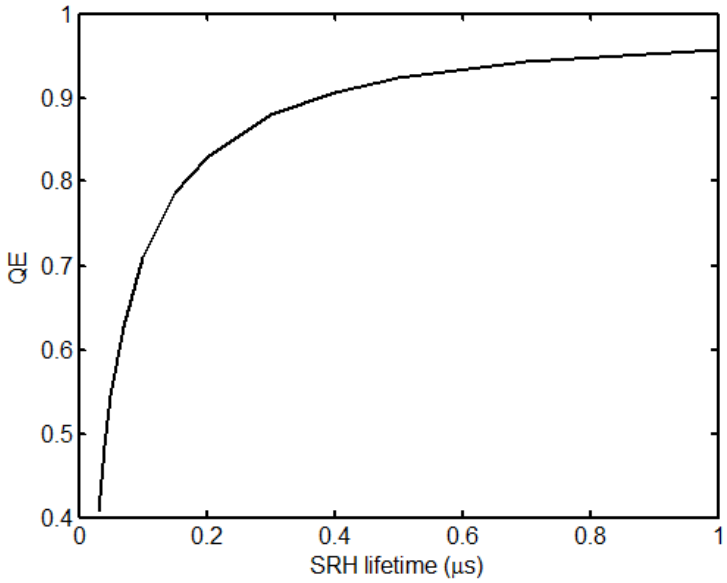

Figure 10: QE vs. SRH lifetime obtained from charge diffusion simulation

Figure 11 and Figure 12 show the lifetime, dark current, and relative response maps over the entire surface of SWIR FPA #2. This FPA has a very degraded region in the upper ~20%. This FPA also has several defects in which the lifetime is low enough to affect the QE and show up in the relative response map. These defects do not show up as strongly in the dark current map indicating that the nature of the defects and impurities varies. Some regions show strong correlation between the lifetime and dark current, but not in the relative response map. Other defects show up in the lifetime and relative response maps but not as strongly in the dark current map.

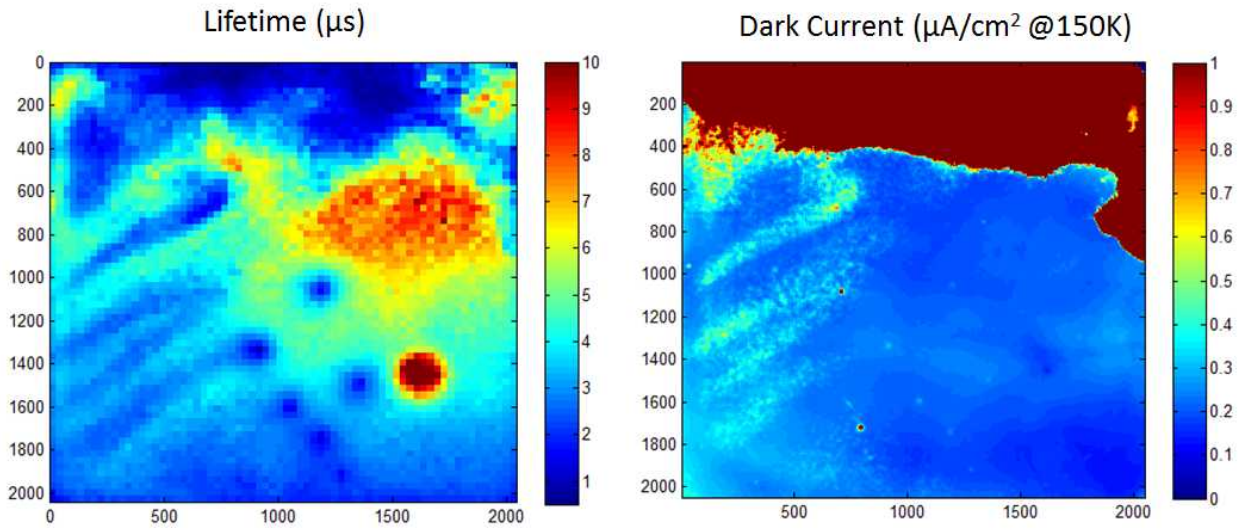

Figure 11: Lifetime and dark current map for SWIR FPA #2

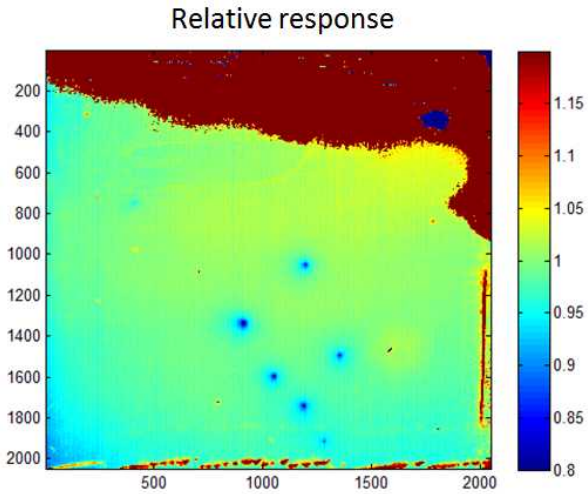

Figure 12: Lifetime and relative response map for SWIR FPA #2

Figure 13 shows the lifetime and dark current map over the entire surface of MWIR FPA #1. This FPA also shows strong correlation between SRH lifetime and dark current. There were no defects affecting the QE for this FPA. A high resolution scan over an area with dense spatial features is shown in Figure 14.

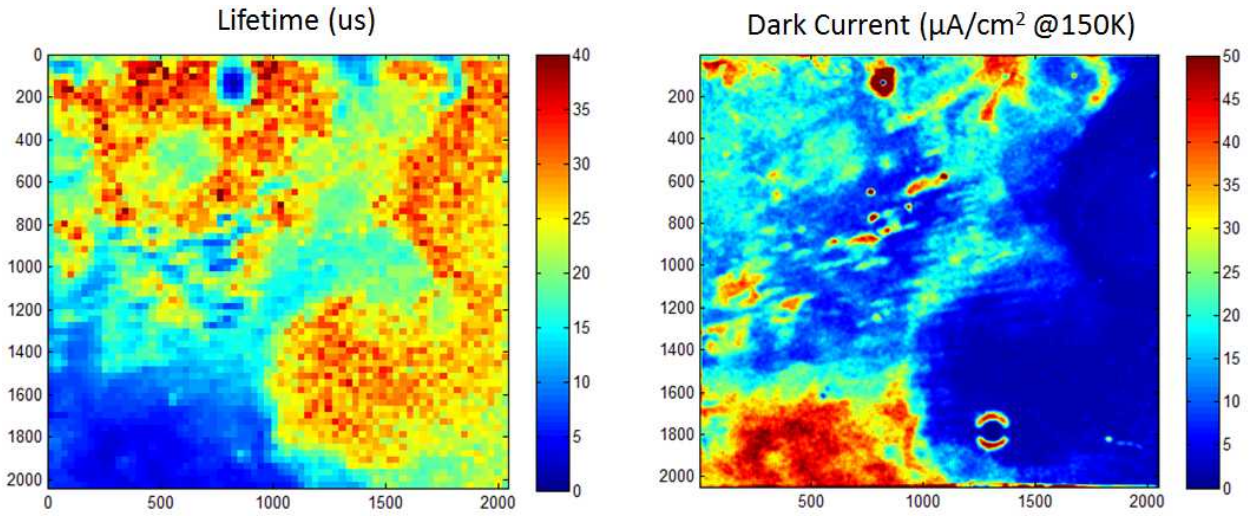

Figure 13: Lifetime and dark current map for MWIR FPA #1

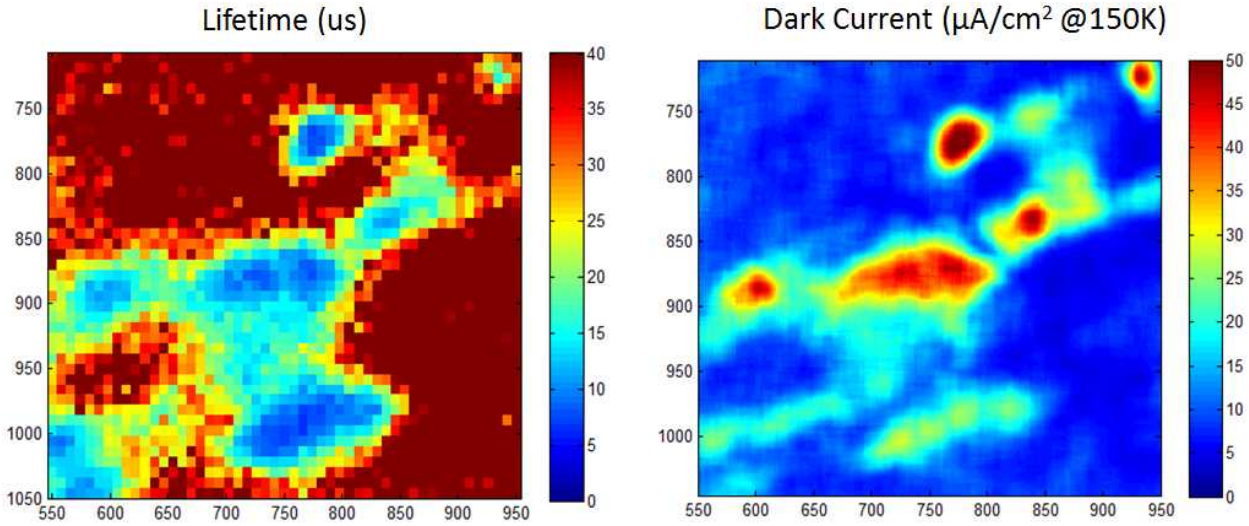

Figure 14: High resolution (0.15mm spot size) lifetime map and corresponding dark current map for an area of interest on MWIR FPA #1

Figure 15 shows the lifetime and dark current map over the entire surface of MWIR FPA #2. This FPA has much more uniformly high lifetime and low dark current regions than the others. It does have some very sharp defects and features towards the bottom right.

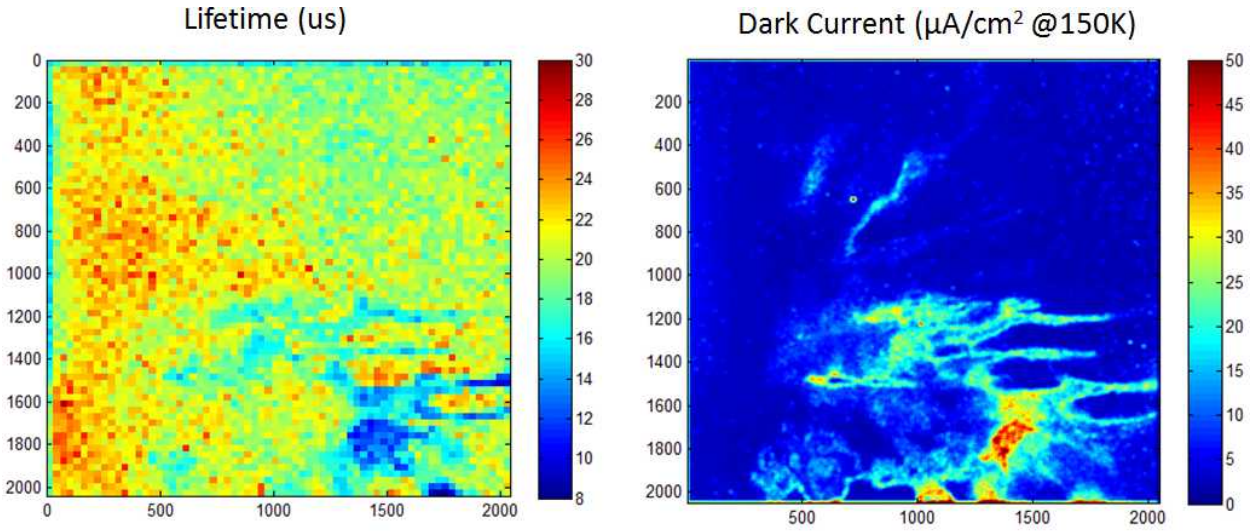

Figure 15: Lifetime and dark current map for MWIR FPA #2

3.0 Summary

These measurement and analysis techniques are very powerful in that the measurement is taken passively with the device unpowered. It could be performed on a material sample wafer to test material quality during any stage of the fabrication process. This can be used to gain some insight on when and how impurities and defects form in the material. This study was performed on fully hybridized FPAs because the dark current and relative response are easily obtained for comparison with lifetime measurements. The FPAs were known to be severely degraded which provided a diverse variety of defective areas to test. The strong correlations found between SRH lifetime, dark current, and relative response can allow us to make inferences about the performance of candidate wafers and detectors before hybridization.

4.0 References

[1]B. Streetman and S Banerjee, *Solid State Electronic Devices* Prentice Hall, Upper Saddle River, NJ, 2000.

[2]S. Sze and K. Ng, *Physics of Semiconductor Devices* John Wiley & Sons, Hoboken, NJ, 2007.

[3] S. Rein, *Lifetime Spectroscopy* Springer Berlin Heidelberg, Germany, 2005

[4] Hansen et all, "Energy gap versus alloy composition and temperature in $Hg_{(1-x)}Cd_{(x)}Te$", *J. Appl. Phys.* **1982**, 53, 7099-7101.

[5] G.L. Hansen and J.L. Schmidt, "Calculation of intrinsic carrier concentration in $Hg_{(1-x)}Cd_{(x)}Te$", *J. Appl. Phys.* **1983**, 54, 1639-1640.

[6] P.K. Saxena, "Modeling and simulation of HgCdTe based p^+-n-n^+ LWIR photodetector", *Infrared Physics and Technology* **2011**, 54, 25-33.

[7] A Itsuno, J. Phillips, and S. Velicu, "Predicted performance improvement of auger-suppressed

HgCdTe photodiodes and p-n heterojunction detectors", *IEEE Transactions on Electron Devices* **2011**, 58, 501-507.